SCIENTIFIC REP♥RTS

OPEN

Effect of halide-mixing on the switching behaviors of organic-inorganic hybrid perovskite memory

Bohee Hwang[1], Chungwan Gu[1], Donghwa Lee[2] & Jang-Sik Lee[1]

Mixed halide perovskite materials are actively researched for solar cells with high efficiency. Their hysteresis which originates from the movement of defects make perovskite a candidate for resistive switching memory devices. We demonstrate the resistive switching device based on mixed-halide organic-inorganic hybrid perovskite $CH_3NH_3PbI_{3-x}Br_x$ ($x = 0, 1, 2, 3$). Solvent engineering is used to deposit the homogeneous $CH_3NH_3PbI_{3-x}Br_x$ layer on the indium-tin oxide-coated glass substrates. The memory device based on $CH_3NH_3PbI_{3-x}Br_x$ exhibits write endurance and long retention, which indicate reproducible and reliable memory properties. According to the increase in Br contents in $CH_3NH_3PbI_{3-x}Br_x$ the set electric field required to make the device from low resistance state to high resistance state decreases. This result is in accord with the theoretical calculation of migration barriers, that is the barrier to ionic migration in perovskites is found to be lower for Br^- (0.23 eV) than for I^- (0.29–0.30 eV). The resistive switching may be the result of halide vacancy defects and formation of conductive filaments under electric field in the mixed perovskite layer. It is observed that enhancement in operating voltage can be achieved by controlling the halide contents in the film.

Resistive switching random access memory (ReRAM) is a promising nonvolatile memory device due to its scalability, fast operation time, high density and low power consumption[1–3]. ReRAM stores information as two resistance states: high resistance state (HRS) and low resistance state (LRS). Numerous materials such as organics[4,5], binary oxides[6,7], and perovskite oxides[8–10] have exhibited switchable resistance. Especially, ReRAMs based on inorganic perovskite oxide materials (e.g., $Pr_{0.7}Ca_{0.3}MnO_3$ (PCMO)[8], $SrTiO_3$ (STO)[9] and $SrZrO_3$:Cr. (SZO:Cr)[10]) have been investigated.

Organic-inorganic perovskite materials including mixed halide perovskites are promising materials in electronic and optoelectronic devices including photodetectors[11], light-emitting diodes[12], and lasers[13] in addition to solar cell applications[14,15]. Also, this material shows hysteresis in current-voltage responses due to defect drift or ion migration. Utilizing the defects in the organic-inorganic perovskite materials extends the application to memory devices[16–20]. Moreover, mixed halide perovskites have been investigated from several studies to improve the property of $CH_3NH_3PbI_3$, such as enhancing carrier transport[21]. For example, $CH_3NH_3PbI_{3-x}Br_x$ exhibited improved carrier mobility and decreased recombination rate, and this feature can be used to fabricate low power consumption memory device due to efficient charge transport.

We selected organic-inorganic hybrid perovskite ($CH_3NH_3PbI_{3-x}Br_x$, $x = 0, 1, 2, 3$) to evaluate its suitability for resistive switching memory. Use of this perovskite in ReRAM is viable for three reasons. (1) $CH_3NH_3PbI_{3-x}Br_x$ exhibits hysteresis in current-voltage (I-V) curve in solar cell as a result of ion or defect migration[22,23]. Reaction of a charge carrier with a defect can lead to a formation of conductive filament that influences the change of the resistance state. (2) $CH_3NH_3PbI_{3-x}Br_x$ can be cast as uniform films by simple solution processing. Especially, solvent-engineering technology[24,25] leads to a homogeneous and dense film. (3) The activation barrier for ionic migration is lower for Br^- than for I^-[26]. As a consequence, this may lead to improved operating voltage and switching speed. This motivated to include Br in $CH_3NH_3PbI_3$.

[1]Department of Materials Science and Engineering, Pohang University of Science and Technology (POSTECH), Pohang, 790-784, Korea. [2]School of Materials Science and Engineering, Chonnam National University, 77 Yongbongro, Buk-gu, Gwangju, 500-757, Korea. Correspondence and requests for materials should be addressed to J.-S.L. (email: jangsik@postech.ac.kr)

Improving operating voltage of MAPbI$_3$ has been achieved by substitution of I$^-$ with Br$^-$, which arises from low activation barrier of Br vacancy. In this study, we evaluate CH$_3$NH$_3$PbI$_{3-x}$Br$_x$ as a component in nonvolatile memory devices. We also quantified how Br incorporation affects the electrical properties of different compositions of CH$_3$NH$_3$PbI$_{3-x}$Br$_x$ (x = 0, 1, 2, 3). The fabricated Au/CH$_3$NH$_3$PbI$_{3-x}$Br$_x$/ITO memory device shows low voltage operation, long data retention, and good endurance. Based on measured current electric field responses, we propose possible resistive switching mechanisms that involve migration of Br$^-$ and I$^-$ vacancies. We demonstrated first-principles density functional theory (DFT) calculations to clarify the lower ionic migration barrier for bromide vacancy than for iodine vacancy which leads to decreased electric field as Br content increases. Based on our present results, it is promising that the ReRAM property with CH$_3$NH$_3$PbI$_{3-x}$Br$_x$ can be improved by controlling the Br contents.

Experimental Section

Synthesis of CH$_3$NH$_3$I and CH$_3$NH$_3$Br.
CH$_3$NH$_3$I and CH$_3$NH$_3$Br were synthesized from HI (57 wt% in water, Aldrich) or HBr respectively, by mixing them with CH$_3$NH$_2$ (40% in water, Aldrich) in 1:1 molar ratio. The reaction was performed in an ice bath under stirring for 6 h in a ventilation hood, then the solvent of the resulting solution was removed using a rotary evaporator for 1 h at 65 °C. MAI and MABr powder that precipitated during evaporation were washed with diethyl ether three times to remove residual impurities. The resulting white powder was dried in a vacuum oven, then dissolved in ethanol and recrystallized from diethyl ether. The powder was filtered using a vacuum pump then dried again in a vacuum oven[25].

Perovskite deposition and device fabrication.
PbI$_2$ and CH$_3$NH$_3$I were dissolved in N, N-dimethlylformamide (DMF) to obtain 30 wt% CH$_3$NH$_3$PbI$_3$. PbBr$_2$ and CH$_3$NH$_3$Br were dissolved in DMF to obtain 30 wt% CH$_3$NH$_3$PbBr$_3$. The CH$_3$NH$_3$PbI$_{3-x}$Br$_x$ solutions were made by stoichiometric mixing 1:1 molar ratios of CH$_3$NH$_3$Br or CH$_3$NH$_3$I with PbI$_2$ or PbBr$_2$. The solution was stirred overnight at 70 °C under N$_2$ environment. Before device fabrication, ITO/glass substrate was cleaned with isopropyl alcohol, and deionized water, then treated using UV/O$_3$ (wavelength = 253.7 nm and 184.9 nm). The solution was spin coated on the ITO/glass at 7,000 rpm for 50 s. After delay time, toluene was quickly dropped onto the center of the substrate during spin coating. The obtained films were annealed at 110 °C for 15 min under N$_2$ environment to eliminate residual solvents. Finally dot-shaped Au electrodes were deposited on the perovskite layer by evaporation through a shadow mask.

Characterization.
UV-vis spectrophotometer (Cary 100, Agilent Technologies) was used to characterize CH$_3$NH$_3$PbI$_{3-x}$Br$_x$ perovskite film. Morphological images of surface and cross section were captured using high-resolution FE-SEM (JEOL) with 10-kV acceleration voltage. Crystal structure was measured using XRD (Rigaku D/MAX-2500) with Cu Kα radiation at a step size of 0.02°. Current-voltage characteristics were measured using a Keithley 4200 in the vacuum probe station; the voltage was controlled by one of the Au electrodes under dc sweeping voltage applied as 0 V → 2 V → 0 V → −1.5 V → 0 V and the bottom electrode (ITO) was grounded.

Results and Discussion

Au/CH$_3$NH$_3$PbI$_{3-x}$Br$_x$/ITO-coated glass is used to demonstrate memory devices that have a metal/insulator/metal (MIM) structure. (Fig. 1a) Through the replacement of I$^-$ with Br$^-$, the color of the film changed from semi-transparent dark brown (CH$_3$NH$_3$PbI$_3$) to light brown (CH$_3$NH$_3$PbI$_2$Br, CH$_3$NH$_3$PbIBr$_2$) then to yellow (CH$_3$NH$_3$PbBr$_3$) with increasing Br content. (Fig. 1b). The absorbtion band edge of CH$_3$NH$_3$PbI$_{3-x}$Br$_x$ (x = 0, 1, 2, 3) can be tuned from a 780.20 nm wavelength (1.58 eV) to 542.82 nm wavelength (2.28 eV) (Fig. 1c). Increasing the Br content in the perovskite, the absorption band of perovskite film shifts to shorter wavelength, which indicates that energy band gap (E$_g$) can be changed by the composition. The band gap values of CH$_3$NH$_3$PbI$_{3-x}$Br$_x$ (x = 0, 1, 2, 3) are consistent with previous reports[27]. The X-ray diffraction patterns (XRD) of CH$_3$NH$_3$PbI$_{3-x}$Br$_x$ (x = 0, 1, 2, 3) showed in 2θ range of 13.5–16° (Fig. 1d). The bottom XRD patterns of CH$_3$NH$_3$PbI$_3$ exhibit peaks at 14.18°, 28.48°, and 31.96° which can be indexed to (110), (220), and (310) planes, respectively. This tetragonal structure of CH$_3$NH$_3$PbI$_3$ indicates lattice constants with a = 8.855 Å and c = 12.659 Å calculated using the Bragg equation[28]. The top XRD patterns of CH$_3$NH$_3$PbBr$_3$ indicated cubic perovskite phase which presented the peaks at 15°, 30.18°, and 45.92° which can be assigned to (100), (200) and (300) planes, respectively. (Figure S1a) The tetragonal phase of CH$_3$NH$_3$PbI$_3$ remained until x = 1 and then changed to cubic phase around x = 2.[27] As the tetragonal phase of CH$_3$NH$_3$PbI$_3$ transited to cubic phase of CH$_3$NH$_3$PbBr$_3$, the PbX$_6$ octahedron rotated along the ⟨001⟩ axis which remaining connected with corner-shared octahedron, and this lead to pseudocubic lattice[27,29]. In CH$_3$NH$_3$PbI$_3$, the main (110) diffraction peak of perovskite occurs at 14.18°; as Br$^-$ progressively replaced I$^-$ in CH$_3$NH$_3$PbI$_3$, this diffraction peak shifted to 14.44° in CH$_3$NH$_3$PbI$_2$Br, 14.66° in CH$_3$NH$_3$PbIBr$_2$, and 14.98° in CH$_3$NH$_3$PbBr$_3$. This peak shift occurs because replacing larger I atoms with smaller Br atoms decreases the lattice spacing. As the Br content increased, the tetragonal lattice parameter a, c decrease almost linearly (Figure S1b). The pseudocubic lattice parameter a was calculated, which decreased from 6.23 Å to 5.91 Å when the Br content increased. (Figure S1c)[29] This result is in accordance with the Vegard's law, which states that a varies linearly in the absence of a strong electronic effect[30]. CH$_3$NH$_3$PbI$_3$, CH$_3$NH$_3$PbI$_2$Br, CH$_3$NH$_3$PbIBr$_2$, and CH$_3$NH$_3$PbBr$_3$ deposited on ITO-coated glass substrate showed uniform layer of perovskite films which were obtained from cross-sectional SEM measurement (Fig. 2).

Current-Electrical field (I- F$_E$) curves (Fig. 3a) in the Au/Perovskite/ITO devices exhibit bipolar resistive switching under compliance current (CC) of = 1 mA. In this work we used electric field (F$_E$ = V/t (thickness of perovskite layers)) instead of applied bias (V) for comparison since there is a slight difference in thicknesses of perovskite layers with different halide composition. Ion migration depended on F$_E$. During the first voltage sweep
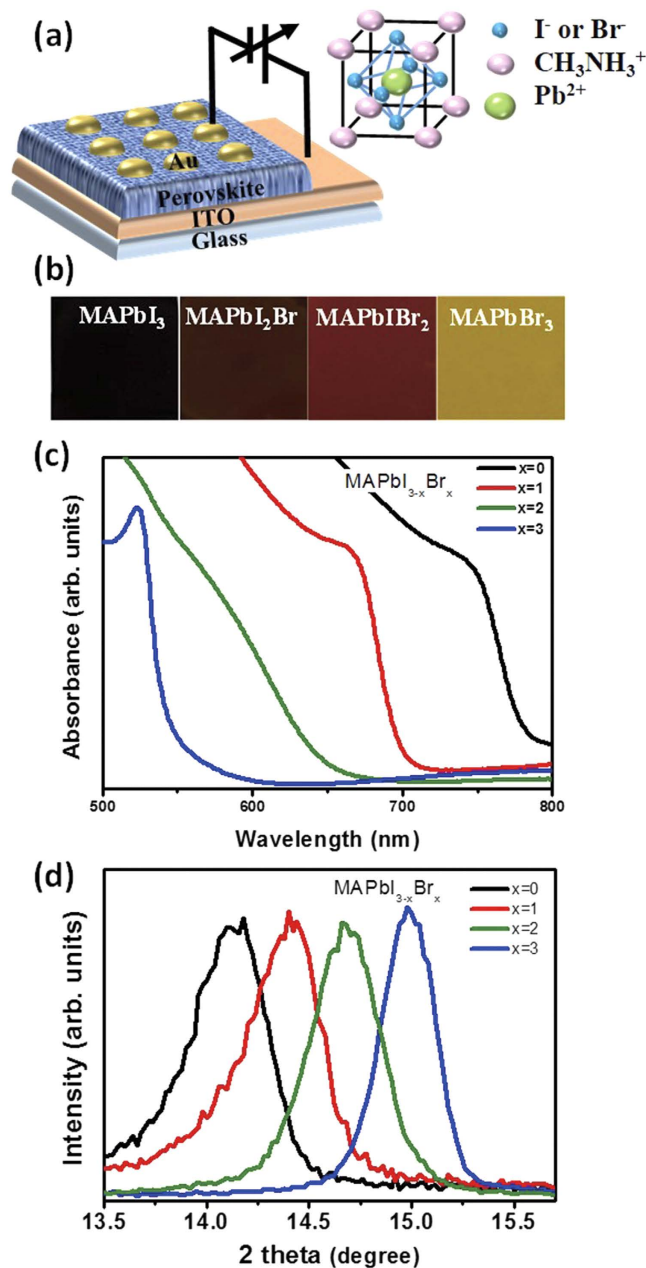
Figure 1. Hybrid organic-inorganic perovskite resistive switching memory devices. (**a**) Schematic diagram of memory device with a structure of Au (top electrode)/hybrid perovskite layer/ITO (bottom electrode)/glass substrate. (Right figure: schematic perovskite structure). (**b**) Photographs of $CH_3NH_3PbI_{3-x}Br_x$ films. (**c**) UV-vis absorption spectra of $CH_3NH_3PbI_{3-x}Br_x$ films. (**d**) X-ray diffraction pattern of hybrid perovskite layer with different Br^- ion contents to show shift of (110) peaks.

on $CH_3NH_3PbI_3$ at positive bias from zero to set F_E ($F_{E\,set} \sim 9.41 \times 10^4$ V/cm), the resistance state changed from HRS (OFF state) to LRS (ON state). When a negative F_E was applied, the current decreased gradually at $F_E < -2.79 \times 10^4$ V/cm; the resistance changed from LRS to HRS. F_E at which resistance changed from HRS to LRS was lowest on $CH_3NH_3PbBr_3$, which means that the ions or defects in $CH_3NH_3PbBr_3$ move easily in the film.

Many types of defects (e.g., vacancies, interstitials, cation substitutions, antisite substitutions) can influence the switching behaviors in perovskites. Bromide vacancies ($V^\bullet_{Br}$), lead vacancies (V''_{Pb}), and CH_3NH_3 vacancies (V'_{MA}, where MA = methylammonium = CH_3NH_3) have relatively low formation energy[31,32], so other interstitials or antisite defects are not likely to influence the perovskite film. Also, in a previous study, the lowest activation energy E_A determines the rate of vacancy migration in the perovskite film, and $V^\bullet_{Br}$ has the lowest E_A for ionic migration[26]. The 'set' electric fields of devices decreased as Br content increased. (Fig. 3b) Moreover, cell-to-cell properties based on the 10 individual devices of $CH_3NH_3PbI_{3-x}Br_x$ film showed same trend such as increasing Br content leads to lower set electric field. (Figure S2) Because the $V^\bullet_{Br}$ has the lowest E_A, $V^\bullet_{Br}$ may be easier to be moved to the electrode to form a conductive filament in the $CH_3NH_3PbBr_3$ film. To confirm the

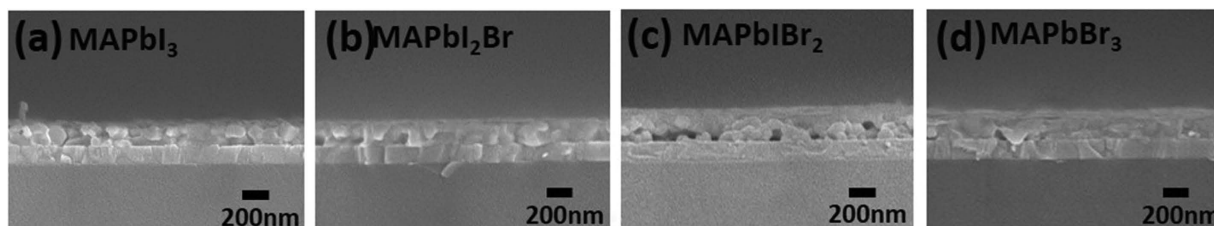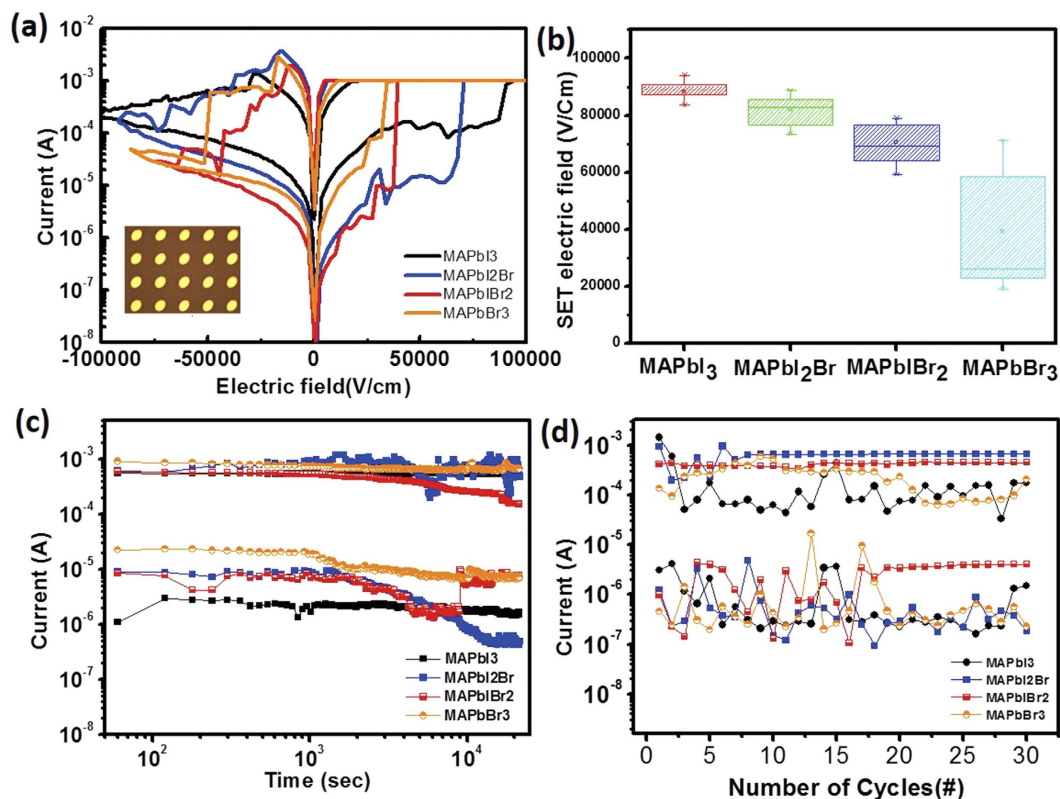**Figure 2. SEM images of cross-sectional views (a to d) of $CH_3NH_3PbI_{3-x}Br_x$ ($x = 0, 1, 2, 3$) layers.**

Figure 3. Resistive switching of $Au/CH_3NH_3PbI_{3-x}Br_x/ITO$. (**a**) I-V characteristics of Au/perovskite/ITO structure (inset: top view of memory device). (**b**) Statistical distribution of set electric fields of the hybrid perovskite resistive switching memory. (**c**) Data retention characteristics of LRS and HRS states at room temperature. (**d**) Switching endurance of perovskite memory device.

conduction mechanisms of $Au/CH_3NH_3PbI_3$ (or $CH_3NH_3PbBr_3$)/ITO-coated glass structured ReRAM devices, a double logarithmic plot of the I-V curves is obtained (Figure S3). The conduction mechanism of the film is space-charge-limited conduction (SCLC) during HRS ($I \propto V^2$) and filamentary type during LRS (Figure S3a,e)[33]. Intrinsic atomic defects in perovskite film, such as $V^{\bullet}_I$, $V"_{Pb}$, V'_{MA}, act as the trap sites[34] which can be SCLC traps. Iodide vacancy which is the dominant vacancy explaining switching mechanism forms the shallow level acting as a trap site near conduction band, and these defects trap charge carriers. When the positive bias is applied, the I-V curves in the HRS region consist of two different linear regions: at low voltage ($<0.3\,V$) the curves are linear(Ohmic conduction), while at high voltage ($>0.3\,V$) it presents quadratic region until the set voltage was reached. (Figure S3a) At $0\sim0.3\,V$, the quantity of injected carriers is lower than that of thermally generated free charge carriers and the curve follows ohmic behavior due to partially filled traps. At high voltage ($>0.3\,V$) during the voltage change from Ohmic to SCLC, all traps are occupied by charge carriers because of sufficient electric field, and the conduction curve obeys $I \propto V^2$. In $MAPbBr_3$ film, the logarithmic I-V curve in LRS is similar to the LRS of $MAPbI_3$ that also shows ohmic conduction. (Figure S3b) Applying the bias on the $MAPbBr_3$ film from 0 to 2 V changed the conduction from ohmic to SCLC in the HRS region. Through SCLC transport in I-V curves, charge trapping sites that may be formed in perovskite layer[15] can be responsible for the resistive switching behavior of Au/perovskite/ITO device which will be explained in resistive switching mechanism.

The data retention property was evaluated to test the stability of the memory device with a reading voltage of $0.2\,V$ at room temperature (Fig. 3c). A constant ON/OFF ratio of $\sim10^2$ was achieved for 2×10^4 s. The current
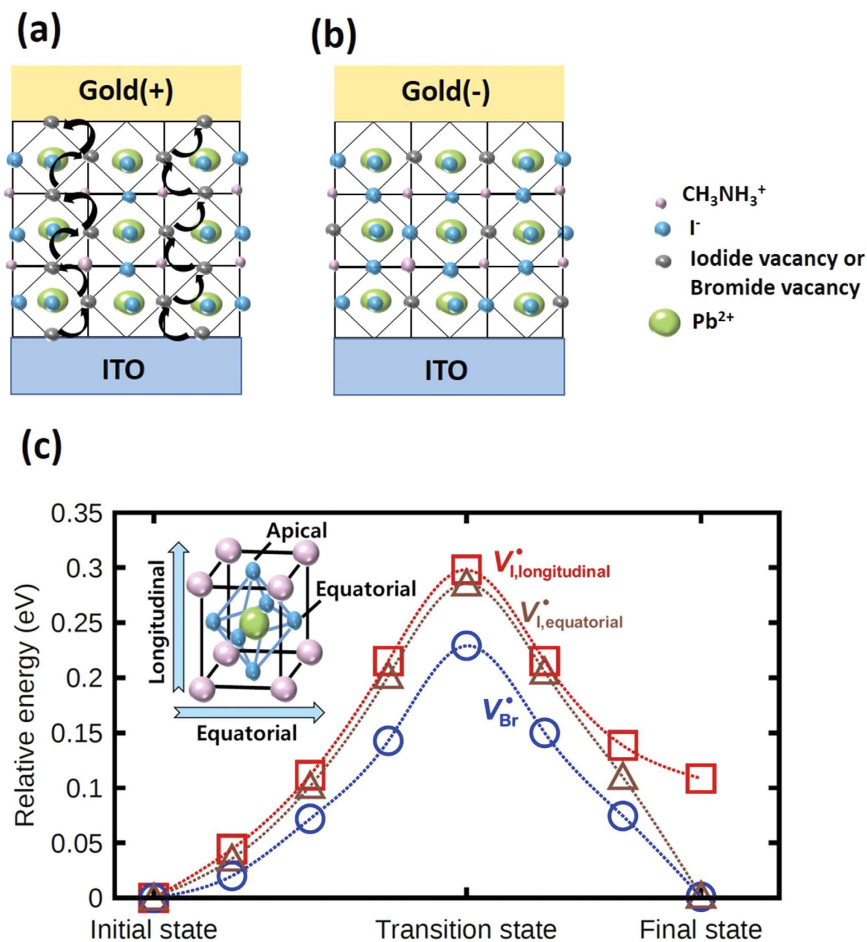
Figure 4. Proposed resistive switching mechanism of perovskite ($CH_3NH_3PbI_{3-x}Br_x$)-based RRAM devices. (**a**) Iodide (or Bromide) vacancy connected with top and bottom electrodes under positive bias to top electrode. (**b**) Rupture of filament under negative bias to top electrode. (**c**) Potential energy profile along two migration pathways of $V^\bullet_I$ and one pathway of $V^\bullet_{Br}$ in tetragonal $CH_3NH_3PbI_3$ and cubic $CH_3NH_3PbBr_3$; two energy profiles of $V^\bullet_I$ are shown as longitudinal (red square) and equatorial (brown triangle) while one energy profile of $V^\bullet_{Br}$ is shown as blue circle. Inset figure shows the schematic view of two migration pathways in tetragonal $CH_3NH_3PbI_3$.

fluctuated in the HRS region but the ON/OFF ratio was maintained overall. This fluctuation is caused by charge trapping and detrapping in various trap states created by defects at different distances from the electrode[35].

The cycling endurances of Au/perovskite/ITO devices were measured using consecutive ac voltage pulses under $V_{set} = +2\,V$ and $V_{reset} = -2\,V$ to evaluate the electrical stability (Fig. 3d). The measured voltage was 0.2 V. The endurance characteristics varied slightly over time, but neither LRS nor HRS degraded. We conclude that Au/perovskite/ITO devices are uniform and reliable. Moreover, we compared set electric field and ON/OFF ratio of our device with devices based on inorganic perovskites and organic-inorganic perovskites. Inorganic perovskites, such as V-doped $SrZrO_3$ or $Pr_{0.7}Ca_{0.3}MnO_3$, showed varied set electric field and the ON/OFF ratio was around 10^2 or larger than 10^2.[36,37] Our device showed comparable set electric field near $\sim 10^4\,V/cm$ and ON/OFF ratio ($>10^2$) compared with other organic-inorganic perovskite based memory device[16–18]. Though larger ON/OFF ratio leads to low misreading rate with accurate controlling of the ON and OFF states, our device that shows ON/OFF ratio ($>10^2$) is suitable enough to applied to memory applications.

The hysteresis in perovskites occurs under specific scanning conditions[18,38,39]; previous studies have suggested that it is due to migration of I^- ions[40,41] or to charge trapping[42,43]. The switching mechanism of Au/perovskite/ITO may be explained by defect migrations and charge trapping under the electric field (Fig. 4a,b). In order to understand the superior characteristics of $CH_3NH_3PbI_{3-x}Br_x$ with Br content, first-principles density functional theory (DFT) calculations are performed. In this study, we have chosen two compounds, $CH_3NH_3PbI_3$ and $CH_3NH_3PbBr_3$, which has the minimum and maximum Br context. Since the importance of the anion vacancy migration for the switching behavior in ReRAM device has been identified by previous studies[44,45], we have focused our study on the migration behavior of $V^\bullet_I$ and $V^\bullet_{Br}$ in $CH_3NH_3PbI_3$ and $CH_3NH_3PbBr_3$ in order to clarify the decreased set electric field with increased Br content. The potential energy profile along the two migration pathways of $V^\bullet_I$ and one migration pathways of $V^\bullet_{Br}$ are shown (Fig. 4c). For tetragonal $CH_3NH_3PbI_3$, the migration of $V^\bullet_I$ can occur through two different pathways (longitudinal and equatorial) as shown in in-set of Fig. 4c;

the longitudinal pathway is the migration between apical and equatorial positions along the long c-axis of tetragonal cell, while the equatorial pathway represents the migration between equatorial positions along xy-plane of the tetragonal cell. On the other hand, for cubic $CH_3NH_3PbBr_3$, the migration behavior of $V^{\bullet}_{Br}$ can show only one pattern since both pathways are identical. Substantial difference in energetic stability is observed between apical and equatorial positions for tetragonal $CH_3NH_3PbI_3$; Our DFT calculations predict that $V^{\bullet}_{I}$ sitting on the apical position is energetically 0.11 eV higher than that sitting on the equatorial position. (see red line in Fig. 4c) This means that $V^{\bullet}_{I}$ prefers to place on the equatorial position and so the longitudinal migration process occurs from one equatorial position to another by passing through the apical position. As a result, the longitudinal migration accompanies two migration barriers: equatorial to apical (0.30 eV) and apical to equatorial (0.19 eV). Unlike in the case of the longitudinal migration process, the equatorial migration involves only one migration barrier of 0.29 eV between two equatorial positions. (See brown line in Fig. 4c) Thus, in tetragonal $CH_3NH_3PbI_3$, although two migration processes have significantly different energy profiles, both have similar energy barrier (0.29~0.30 eV) for the migration of $V^{\bullet}_{I}$. On the other hand, in cubic $CH_3NH_3PbBr_3$, $V^{\bullet}_{Br}$ goes through only one migration pathway; our DFT calculation predicts the energy barrier of 0.23 eV (Fig. 4c), and this calculation is in good agreement with previous studies which $V^{\bullet}_{Br}$ ($\approx$0.27 eV)[26] has the lowest activation for the defect migration. Since $V^{\bullet}_{Br}$ has lower migration barrier than $V^{\bullet}_{I}$, it is easier to migrate to form a conductive filament. Thus, in the $CH_3NH_3PbI_{3-x}Br_x$, the decreased set electric field with the increased Br content is a result of the enhanced migration of $V^{\bullet}_{Br}$.

Ion migration rate (r_m) in a solid material can be estimated using the Arrhenius relation, $r_m \propto \exp\left(\frac{-E_A}{K_B T}\right)$, where $K_B = 8.617 \times 10^{-5}$ eV/K is the Boltzmann constant, and T [K] is the absolute temperature. Because $V^{\bullet}_{I}$ has the lowest E_A in the $CH_3NH_3PbI_3$[31,32,46], the migration rate of $V^{\bullet}_{I}$ should be large enough that defects can migrate easily in the perovskite film. Also, the jumping distance between pairs of $V^{\bullet}_{I}$ is the shortest; this observation could explain their low E_A. The $V^{\bullet}_{I}$ is closer ($\sim$4.46 Å) to nearest I^- ions located on the edge of the PbI_6^{4-} octaheron, than to the closest $CH_3NH_3^+$ and Pb^{2+} ions ($\sim$6.28 Å)[47]. Because E_A of $V^{\bullet}_{I}$ is low, we suggest that this is the cause of resistive switching behavior in $CH_3NH_3PbI_3$, $CH_3NH_3PbI_2Br$. Though $CH_3NH_3PbI_2Br$ contains $V^{\bullet}_{Br}$, it is not sufficient to form $V^{\bullet}_{Br}$-related conductive filament. In the pristine state without the electric field, vacancies will be spread throughout the perovskite film. Under an electric field, a positively charged $V^{\bullet}_{I}$ migrates toward the electrode (ITO) with a negative bias during the set process. Under positive bias, $V^{\bullet}_{I}$ will take the shortest path along the octahedral edge[46] (Fig. 4a). Then charge carriers injected from the electrode will combine with $V^{\bullet}_{I}$ and neutralize it.

As the applied voltage increases, a $V^{\bullet}_{I}$ moves toward the negatively-biased electrode. Subsequently, combinations of $V^{\bullet}_{I}$ with charge carriers will form $V^{\bullet}_{I}$ filaments that connect the top electrode to the bottom electrode. Also, trap sites formed by Frenkel defects such as V'_{MA}, V''_{Pb}, and $V^{\bullet}_{I}$[48] will be occupied by injected electrons. Under reverse bias, electron detrapping leads to rupture of the conduction filament (Fig. 4b). In the case of $CH_3NH_3PbBr_3$ and $CH_3NH_3PbIBr_2$, $V^{\bullet}_{Br}$ would be the main cause of resistive switching properties due to the lowest E_A of $V^{\bullet}_{Br}$ comparing with $V^{\bullet}_{I}$ which was derived from DFT calculation. Moreover, in $CH_3NH_3PbBr_3$ and $CH_3NH_3PbIBr_2$, the migration pathway is analogous to that in $CH_3NH_3PbI_3$.[26] As the migration pathway of $V^{\bullet}_{Br}$ is similar to $V^{\bullet}_{I}$, $V^{\bullet}_{Br}$ will form conductive filaments by combining with the charge carrier in a similar way to $V^{\bullet}_{Br}$.

Conclusion

We investigated organic-inorganic perovskite ReRAM based on $CH_3NH_3PbI_{3-x}Br_x$ (x = 0, 1, 2, 3) thin films as the resistive switching layer formed by solvent engineering. The memory device fabricated with $CH_3NH_3PbBr_3$ showed the lowest 'set' electric field. The replacement of I with Br decreases the 'set' electric field, and thereby reduces the power consumption of the device. First-principles calculations show that incorporation of Br decreased the 'set' electrical field because compared to a $V^{\bullet}_{I}$, a $V^{\bullet}_{Br}$ has lower E_A and therefore migrates easily in perovskite films. $CH_3NH_3PbBr_3$ perovskite ReRAM showed the lowest operation electric field of about 3.44×10^4 V/cm, long data retention over 10^4 s, and good endurance property. The resistive switching occurs by migration of $V^{\bullet}_{I}$ and $V^{\bullet}_{Br}$, and by formation of conducting filament under electric field. These results indicate that organic-inorganic perovskite materials have potential uses in future memory devices.

References

1. Linn, E., Rosezin, R., Kuegeler, C. & Waser, R. Complementary resistive switches for passive nanocrossbar memories. *Nat. Mater.* **9**, 403–406 (2010).
2. Waser, R. & Aono, M. Nanoionics-based resistive switching memories. *Nat. Mater.* **6**, 833–840 (2007).
3. Waser, R., Dittmann, R., Staikov, G. & Szot, K. Redox-Based Resistive Switching Memories - Nanoionic Mechanisms, Prospects, and Challenges. *Adv. Mater.* **21**, 2632–2663 (2009).
4. Gao, S., Song, C., Chen, C., Zeng, F. & Pan, F. Dynamic Processes of Resistive Switching in Metallic Filament-Based Organic Memory Devices. *J. Phys. Chem. C.* **116**, 17955–17959 (2012).
5. Cho, B. *et al.* Direct Observation of Ag Filamentary Paths in Organic Resistive Memory Devices. *Adv. Funct. Mater.* **21**, 3976–3981 (2011).
6. Yang, J. J. *et al.* Memristive switching mechanism for metal/oxide/metal nanodevices. *Nat. Nanotechnol.* **3**, 429–433 (2008).
7. Kang, B. S. *et al.* High-Current-Density CuO_x/$InZnO_x$Thin-Film Diodes for Cross-Point Memory Applications. *Adv. Mater.* **20**, 3066–3069 (2008).
8. Yasuhara, R., Yamamoto, T., Ohkubo, I., Kumigashira, H. & Oshima, M. Interfacial chemical states of resistance-switching metal/$Pr_{0.7}Ca_{0.3}MnO_3$ interfaces. *Appl. Phys. Lett.* **97**, 132111 (2010).
9. Nili, H. *et al.* Nanoscale Resistive Switching in Amorphous Perovskite Oxide (a-$SrTiO_3$) Memristors. *Adv. Funct. Mater.* **24**, 6741–6750 (2014).
10. Park, J. W., Yang, M. K. & Lee, J. K. Electrode dependence of bipolar resistive switching in $SrZrO_3$: Cr perovskite film-based memory devices. *Electrochem. Solid-State Lett.* **11**, H226–H229 (2008).
11. Dou, L. *et al.* Solution-processed hybrid perovskite photodetectors with high detectivity. *Nat. Commun.* **5**, 5404 (2014).
12. Kim, Y.-H. *et al.* Multicolored Organic/Inorganic Hybrid Perovskite Light-Emitting Diodes. *Adv. Mater.* **27**, 1248–1254 (2015).

13. Zhu, H. *et al.* Lead halide perovskite nanowire lasers with low lasing thresholds and high quality factors. *Nat. Mater.* **14,** 636–642 (2015).

14. Xing, G. *et al.* Long-Range Balanced Electron- and Hole-Transport Lengths in Organic-Inorganic CH₃NH₃PbI₃. *Science* **342,** 344–347 (2013).

15. Stranks, S. D. *et al.* Electron-Hole Diffusion Lengths Exceeding 1 Micrometer in an Organometal Trihalide Perovskite Absorber. *Science* **342,** 341–344 (2013).

16. Wang, C. *et al.* High-efficiency bulk heterojunction memory devices fabricated using organometallic halide perovskite: poly(N-vinylcarbazole) blend active layers. *Dalton Trans.* **45,** 484–488 (2016).

17. Yoo, E. J. *et al.* Resistive Switching Behavior in Organic-Inorganic Hybrid CH₃NH₃PbI₃₋ₓClₓ Perovskite for Resistive Random Access Memory Devices. *Adv. Mater.* **27,** 6170–6175 (2015).

18. Yan, K. *et al.* High-performance perovskite memristor based on methyl ammonium lead halides. *J. Mater. Chem. C* **4,** 1375–1381 (2016).

19. Gu, C. & Lee, J.-S. Flexible Hybrid Organic-Inorganic Perovskite Memory. *ACS Nano* **10,** 5413–5418 (2016).

20. Choi, J. *et al.* Organolead Halide Perovskites for Low Operating Voltage Multilevel Resistive Switching. *Adv. Mater.* **28,** 6562–6567 (2016).

21. Edri, E., Kirmayer, S., Kulbak, M., Hodes, G. & Cahen, D. Chloride Inclusion and Hole Transport Material Doping to Improve Methyl Ammonium Lead Bromide Perovskite-Based High Open-Circuit Voltage Solar Cells. *J. Phys. Chem. Lett.* **5,** 429–433 (2014).

22. Walsh, A., Scanlon, D. O., Chen, S., Gong, X. G. & Wei, S.-H. Self-Regulation Mechanism for Charged Point Defects in Hybrid Halide Perovskites. *Angew. Chem., Int. Ed.* **54,** 1791–1794 (2015).

23. Xiao, Z. *et al.* Giant switchable photovoltaic effect in organometal trihalide perovskite devices. *Nat. Mater.* **14,** 193–198 (2015).

24. Xiao, M. *et al.* A fast deposition-crystallization procedure for highly efficient lead iodide perovskite thin-film solar cells. *Angew. Chem., Int. Ed.* **53,** 9898–9903 (2014).

25. Jeon, N. J. *et al.* Solvent engineering for high-performance inorganic-organic hybrid perovskite solar cells. *Nat. Mater.* **13,** 897–903 (2014).

26. Meloni, S. *et al.* Ionic polarization-induced current-voltage hysteresis in CH₃NH₃PbX₃ perovskite solar cells. *Nat. Commun.* **7,** 10334 (2016).

27. Noh, J. H., Im, S. H., Heo, J. H., Mandal, T. N. & Seok, S. I. Chemical management for colorful, efficient, and stable inorganic-organic hybrid nanostructured solar cells. *Nano Lett.* **13,** 1764–1769 (2013).

28. Kojima, A., Teshima, K., Shirai, Y. & Miyasaka, T. Organometal Halide Perovskites as Visible-Light Sensitizers for Photovoltaic Cells. *J. Am. Chem. Soc.* **131,** 6050–6051 (2009).

29. Poglitsch, A. & Weber, D. Dynamic disorder in methylammoniumtrihalogenoplumbates (II) observed by millimeter-wave spectroscopy. *J. Chem. Phys.* **87,** 6373–6378 (1987).

30. Xu, J. *et al.* Synthesis of Homogeneously Alloyed Cu₂₋ₓ(SᵧSe₁₋ᵧ) Nanowire Bundles with Tunable Compositions and Bandgaps. *Adv. Funct. Mater.* **20,** 4190–4195 (2010).

31. Yu, H., Lu, H., Xie, F., Zhou, S. & Zhao, N. Native Defect-Induced Hysteresis Behavior in Organolead Iodide Perovskite Solar Cells. *Adv. Funct. Mater.* **26,** 1411–1419 (2016).

32. Azpiroz, J. M., Mosconi, E., Bisquert, J. & De Angelis, F. Defect migration in methylammonium lead iodide and its role in perovskite solar cell operation. *Energy Environ. Sci.* **8,** 2118–2127 (2015).

33. Zuo, Q. *et al.* Self-rectifying effect in gold nanocrystal-embedded zirconium oxide resistive memory. *J. Appl. Phys.* **106,** 073724 (2009).

34. Kim, J., Lee, S. H., Lee, J. H. & Hong, K. H. The Role of Intrinsic Defects in Methylammonium Lead Iodide Perovskite. *J. Phys. Chem. Lett.* **5,** 1312–1317 (2014).

35. Sasaki, M. An electron conduction model of resistive memory for resistance dispersion, fluctuation, filament structures, and set/reset mechanism. *J. Appl. Phys.* **112,** 014501 (2012).

36. Li, S. L., Gang, J. L., Li, J., Chu, H. F. & Zheng, D. N. Reproducible low-voltage resistive switching in a low-initial-resistance Pr₀.₇Ca₀.₃MnO₃ junction. *J. Phys. D: Appl. Phys.* **41,** 185409 (2008).

37. Lin, C. C., Tu, B. C., Lin, C. C., Lin, C. H. & Tseng, T. Y. Resistive switching mechanisms of V-doped SrZrO₃ memory films. *IEEE Electron Device Lett.* **27,** 725–727 (2006).

38. Snaith, H. J. *et al.* Anomalous Hysteresis in Perovskite Solar Cells. *J. Phys. Chem. Lett.* **5,** 1511–1515 (2014).

39. Chen, B. *et al.* Impact of Capacitive Effect and Ion Migration on the Hysteretic Behavior of Perovskite Solar Cells. *J. Phys. Chem. Lett.* **6,** 4693–4700 (2015).

40. Haruyama, J., Sodeyama, K., Han, L. & Tateyama, Y. First-Principles Study of Ion Diffusion in Perovskite Solar Cell Sensitizers. *J. Am. Chem. Soc.* **137,** 10048–10051 (2015).

41. Li, C. *et al.* Iodine Migration and its Effect on Hysteresis in Perovskite Solar Cells. *Adv. Mater.* **28,** 2446–2454 (2016).

42. Shao, Y. H., Xiao, Z. G., Bi, C., Yuan, Y. B. & Huang, J. S. Origin and elimination of photocurrent hysteresis by fullerene passivation in CH₃NH₃PbI₃ planar heterojunction solar cells. *Nat. Commun.* **5,** 5784 (2014).

43. Nagaoka, H. *et al.* Zr Incorporation into TiO₂ Electrodes Reduces Hysteresis and Improves Performance in Hybrid Perovskite Solar Cells while Increasing Carrier Lifetimes. *J. Phys. Chem. Lett.* **6,** 669–675 (2015).

44. Yang, J. J. S., Strukov, D. B. & Stewart, D. R. Memristive devices for computing. *Nat. Nanotechnol.* **8,** 13–24 (2013).

45. Chen, C. *et al.* Conductance quantization in oxygen-anion-migration-based resistive switching memory devices. *Appl. Phys. Lett.* **103,** 0435310 (2013).

46. Eames, C. *et al.* Ionic transport in hybrid lead iodide perovskite solar cells. *Nat. Commun.* **6,** 7497 (2015).

47. Yuan, Y. & Huang, J. Ion Migration in Organometal Trihalide Perovskite and Its Impact on Photovoltaic Efficiency and Stability. *Acc. Chem. Res.* **49,** 286–293 (2016).

48. Kim, J., Lee, S. H., Lee, J. H. & Hong, K. H. The Role of Intrinsic Defects in Methylammonium Lead Iodide Perovskite. *J. Phys. Chem. Lett.* **5,** 1312–1317 (2014).

Acknowledgements

Author Contributions

J.S.L. conceived and directed the research. J.S.L., B.H., C.G. designed and planned the experiment. B.H. and C.G. performed the experiment and acquired the data. D.L. performed DFT calculation and wrote relevant part. B.H. and J.S.L. wrote the manuscript.

Additional Information

Supplementary information accompanies this paper at http://www.nature.com/srep

Competing Interests: The authors declare no competing financial interests.

How to cite this article: Hwang, B. *et al.* Effect of halide-mixing on the switching behaviors of organic-inorganic hybrid perovskite memory. *Sci. Rep.* **7**, 43794; doi: 10.1038/srep43794 (2017).

Publisher's note: Springer Nature remains neutral with regard to jurisdictional claims in published maps and institutional affiliations.